Available online at www.sciencedirect.com
ScienceDirect
Journal of the European Ceramic Society 29 (2009) 647–652
www.elsevier.com/locate/jeurceramsoc

Influence of ytterbium- and samarium-oxides codoping on structure and thermal conductivity of zirconate ceramics

Zhan-Guo Liu, Jia-Hu Ouyang *, Yu Zhou, Jing Li, Xiao-Liang Xia

Institute for Advanced Ceramics, Department of Materials Science, Harbin Institute of Technology, PO Box 433, Harbin 150001, China

Received 12 April 2008; received in revised form 11 July 2008; accepted 18 July 2008
Available online 28 August 2008

Abstract

To increase operating temperature and improve performance of gas-turbine engines, it is urgently needed to develop new thermal barrier oxides with a lower thermal conductivity than 6–8 wt.% yttria-stabilized zirconia. $(Yb_xSm_{1-x})_2Zr_2O_7$ $(0 \le x \le 1.0)$ ceramics were synthesized by pressureless-sintered at 1700 °C for 10 h in air. The relative density, phase structure, morphology and thermal diffusivity coefficients of $(Yb_xSm_{1-x})_2Zr_2O_7$ ceramics were investigated by the Archimedes method, X-ray diffraction, scanning electron microscopy and laser-flash method. $Sm_2Zr_2O_7$ and $(Yb_{0.1}Sm_{0.9})_2Zr_2O_7$ ceramics exhibit a pyrochlore structure, while $(Yb_xSm_{1-x})_2Zr_2O_7$ $(0.3 \le x \le 1.0)$ ceramics have a defect fluorite-type structure. The thermal conductivities of $(Yb_xSm_{1-x})_2Zr_2O_7$ ceramics first gradually decrease with increasing temperature, and then increase slightly above 800 °C due to the increased radiation contribution. $YbSmZr_2O_7$ ceramics have the lowest thermal conductivity over the entire temperature range, which is caused by the reduction of cation mean free path in ytterbium–samarium zirconate system.

Keywords: Sintering; Microstructure-final; Thermal conductivity; $(Yb_xSm_{1-x})_2Zr_2O_7$

1. Introduction

Six to 8 wt.% yttria-stabilized zirconia (YSZ) thermal barrier coatings (TBCs), which are generally produced by plasma spraying or electron beam physical vapor deposition, are widely used to provide thermal insulation for hot-section components of superalloys against hot gas streams to enhance operating temperature and improve performance of gas-turbine engines.[1–3] However, 6–8 wt.%YSZ is limited to applications below 1200 °C due to its sintering resistance and phase structure stability during long-term service.[4,5] YSZ TBCs system is currently capable of reducing metal temperature by about 140 °C, whereas potential benefits are estimated to be greater than 170 °C.[6] In order to further increase the operating efficiency, it is urgently needed to develop new thermal barrier oxides with a significantly lower thermal conductivity than YSZ. Two important groups of candidate materials, one based on the co-doping of YSZ with one or more metal oxides and the other on the rare-earth zirconate ceramics, have been developed for modern gas-turbine engines, which are intended to operate at temperatures as high as possible.[7–9]

The rare-earth zirconates with the general formula of $Ln_2Zr_2O_7$ (Ln = rare-earth elements) have a distinctly lower thermal conductivity than 6–8 wt.%YSZ, and exhibit a pyrochlore structure or a defect fluorite-type structure, which is mainly governed by the ionic size difference between Ln and Zr sites.[10] The rare-earth zirconate ceramics have high melting points, and undergo order–disorder transition on heating. However, the order–disorder transformation temperatures for rare-earth zirconate ceramics are quite different, such as 2300 °C for $Nd_2Zr_2O_7$, 2000 °C for $Sm_2Zr_2O_7$ and 1530 °C for $Gd_2Zr_2O_7$, respectively.[11] The thermal conductivities of unitary $Ln_2Zr_2O_7$ (Ln = La, Nd, Sm, Gd, Eu, etc.) ceramics vary from 1.1 to 2.0 $W\,m^{-1}\,K^{-1}$ in certain temperature range, although there are discrepancies among the different studies owing to the presence of significant residual porosity in the nominally dense specimens and the use of different measurement techniques.[9,10,12,13] It was claimed that the substitution on Ln site by other cations in $Ln_2Zr_2O_7$ ceramics led to a low thermal conductivity as contrasted with unitary rare-earth zirconates.[13–15] However, no data on phase structure and thermophysical properties of ytterbium–samarium zirconate

* Corresponding author. Tel.: +86 451 86414291; fax: +86 451 86414291.
E-mail address: ouyangjh@hit.edu.cn (J.-H. Ouyang).

0955-2219/$ – see front matter © 2008 Elsevier Ltd. All rights reserved.
doi:10.1016/j.jeurceramsoc.2008.07.033

system have been reported in the literatures. In this paper, ytterbium–samarium zirconate ceramic powders were synthesized by chemical-coprecipitation and calcination method. They were then pressureless-sintered at 1700 °C in air. The structural evolution and thermal conductivity of ytterbium–samarium zirconate ceramics were analyzed.

2. Experimental procedure

Zirconium oxychloride (Zibo Huantuo Chemical Co. Ltd., China; Analytical), samarium oxide and ytterbium oxide powders (Rare-Chem Hi-Tech Co., Ltd., Huizhou, China; purity ≥99.99%) were chosen as starting materials. Rare-earth oxide powders were heat-treated at 900 °C for 2 h before further using. Ceramic powders of $(Yb_xSm_{1-x})_2Zr_2O_7$ ($x = 0$, 0.1, 0.3, 0.5, 0.7, 0.9, 1.0) were synthesized by chemical-coprecipitation and calcination method. For each composition, the appropriate quantity of rare-earth oxides was dissolved in diluted nitric acid, and zirconium oxychloride was dissolved in distilled water. These solutions were mixed, stirred, filtered and slowly added to dilute ammonium hydrate solution to obtain gel-like precipitates. These gels were washed with distilled water for several times, and then washed in analytically pure alcohol. These precipitates were dried, and the residual calcined at 800 °C for 5 h in air. The obtained powders were compacted by cold isostatic pressing at 280 MPa for 5 min. Finally, the compacts were pressureless-sintered at 1700 °C for 10 h in air.

The phases of sintered bulk ceramics were characterized by X-ray diffraction (XRD, Rigaku D/Max 2200VPC, Japan) with Cu Kα radiation at a scan rate of 4°/min at room temperature. The diffraction peaks of $(3\,1\,1)_F/(6\,2\,2)_{Py}$ were also recorded in a step scan mode with a step-width of 0.02°and a step-time of 3 s. In order to evaluate the lattice constant, the silicon powder was used as the calibration reference. The bulk density of the samples was measured by the Archimedes method with an immersion medium of deionized water. The theoretical density of each composition was calculated using lattice parameters acquired from XRD results and the molecular weight in an elementary cell. The microstructure of sintered specimens was observed by scanning electron microscopy (SEM, Hitachi S-4700, Japan). For SEM observations, the specimens were polished with 1 μm diamond paste, and then thermally etched at 1600 °C for 1 h in air before a thin carbon coating was evaporated onto the surfaces of specimens for electrical conductivity. Qualitative X-ray elemental analysis of specimens was carried out using scanning electron microscope (SEM) equipped with energy dispersive spectroscopy (EDS).

The measurement of thermal diffusivity was carried out in argon gas atmosphere using the laser-flash apparatus (Netzsch LFA 427, Germany). The flash source is a neodymium: gallium–gadolinium–garnet (Nd: GGG) laser with a wavelength of 1064 nm, a working voltage of 450 V and a pulse duration of 0.8 ms. Cylindrical disc-shaped samples with a diameter of 12.7 mm and a thickness of 1.5 mm were obtained from the sintered specimens and ground so that both surfaces were coplanar. The thermal diffusivity measurements were made from room temperature to 1400 °C at a temperature interval of 200 °C at atmospheric pressure. To enhance the absorption and emission of the laser beam, both the front and the rear surfaces of the specimens were coated with a thin layer of colloidal graphite. Each specimen was heated in a graphite furnace and the temperature was measured with a W–3%Re/W–25%Re thermocouple. Each sample was measured three times at selected temperatures. During measuring, the front surface of the sample was irradiated with laser beam, which provided an instantaneous energy pulse. The laser energy was absorbed by the front surface of the sample and travelled through the sample. The temperature at the rear surface of the sample was immediately monitored by using an In–Sb detector. The thermal diffusivity was calculated by using the rear surface temperature *vs*. time trace. The experimental uncertainty was estimated to be less than 5%. The specific heat capacities were calculated as a function of temperature from the chemical compositions of $(Yb_xSm_{1-x})_2Zr_2O_7$ ceramics with the Neumann–Kopp rule[16] and the heat capacity data of the constituent oxides (Yb_2O_3, Sm_2O_3 and ZrO_2) obtained from the literature.[17]

The thermal conductivity k ($W\,m^{-1}\,K^{-1}$) is given by Eq. (1) with the heat capacity C_p ($J\,g^{-1}\,K^{-1}$), density ρ ($g\,cm^{-3}$) and thermal diffusivity λ ($mm^2\,s^{-1}$):

$$k = C_p \lambda \rho \tag{1}$$

Because all specimens were not fully dense, the measured thermal conductivity data were corrected for the residual porosity φ of the specimens, using the following equation[10]:

$$\frac{k}{k_0} = 1 - \frac{4}{3}\varphi \tag{2}$$

where k_0 is the corrected thermal conductivity for fully dense materials.

3. Results and discussion

3.1. Densification, phase constituent and microstructure

Fig. 1(a) reveals the X-ray diffraction patterns of $(Yb_xSm_{1-x})_2Zr_2O_7$ ceramics. It can be seen that all $(Yb_xSm_{1-x})_2Zr_2O_7$ ceramics are with a single-phase structure. From Fig. 1(a), $Sm_2Zr_2O_7$ and $(Yb_{0.1}Sm_{0.9})_2Zr_2O_7$ ceramics exhibit a pyrochlore structure, which is characterized by the presence of typical super-lattice peaks at 2θ values of about 14° (1 1 1), 28° (3 1 1), 37° (3 3 1) and 45° (5 1 1) using Cu Kα radiation.[18–20] With the incorporation of smaller Yb^{3+} cations partially instead of larger Sm^{3+} cations, $(Yb_xSm_{1-x})_2Zr_2O_7$ ($0.3 \le x \le 1.0$) ceramics transform into a defect fluorite-type structure.

In the $Ln_2Zr_2O_7$ system, the phase structure is mainly governed by the ionic radius ratio of $r(Ln^{3+})/r(Zr^{4+})$. The stability of pyrochlore structure in zirconates at an atmospheric pressure is limited to the range of $1.46 \le r(Ln^{3+})/r(Zr^{4+}) \le 1.78$.[21] Below 1.46, the array of unoccupied anion sites disorders, to produce a defect-fluorite structure. Above 1.78, there is a transition to a monoclinic phase with $La_2Ti_2O_7$-type structure. The ionic radius of Zr^{4+} is 0.72 Å in the sixfold coordination; however, the ionic radius of Yb^{3+} and Sm^{3+} are 0.985 and 1.079 Å in the

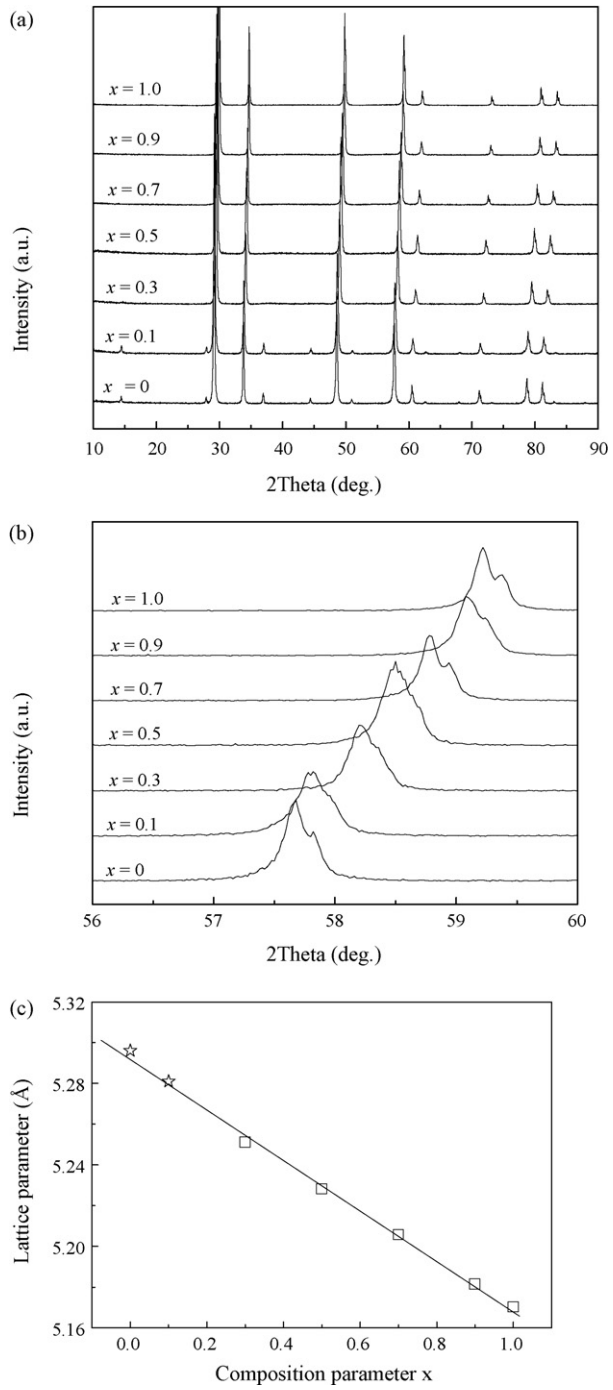

Fig. 1. X-ray diffraction patterns and derived lattice parameters of $(Yb_xSm_{1-x})_2Zr_2O_7$ ceramics: (a) in the 2θ range of 10–90°; (b) a single $(3\,1\,1)_F/(6\,2\,2)_{Py}$ peak in a 2θ range of 56–60°; (c) lattice parameters derived from (b) above. The symbol (☆) in (c) marks the composition with a pyrochlore structure.

eightfold coordination, respectively.[22] The average ionic radius, $r(Ln_{av.}{}^{3+})$, of the Ln-sites in the $(Yb_xSm_{1-x})_2Zr_2O_7$ system is estimated from the ionic radius of the component ions and the chemical composition using the following equation[23]:

$$r(Ln_{av.}^{3+}) = x\, r(Yb^{3+}) + (1-x)\, r(Sm^{3+}) \quad (3)$$

For $Sm_2Zr_2O_7$ and $(Yb_{0.1}Sm_{0.9})_2Zr_2O_7$ ceramics, the values of $r(Ln^{3+})/r(Zr^{4+})$ are equal to 1.50 and 1.48, respectively.

Table 1
Relative densities of $(Yb_xSm_{1-x})_2Zr_2O_7$ ceramics sintered at 1700 °C for 10 h

Ceramic bulk materials	Measured density (g cm^{-3})	Theoretical density (g cm^{-3})	Relative density (%)
$Sm_2Zr_2O_7$	6.494	6.654	97.6
$(Yb_{0.1}Sm_{0.9})_2Zr_2O_7$	6.525	6.762	96.5
$(Yb_{0.3}Sm_{0.7})_2Zr_2O_7$	6.642	6.970	95.3
$(Yb_{0.5}Sm_{0.5})_2Zr_2O_7$	6.936	7.178	96.6
$(Yb_{0.7}Sm_{0.3})_2Zr_2O_7$	7.156	7.385	96.9
$(Yb_{0.9}Sm_{0.1})_2Zr_2O_7$	7.315	7.593	96.3
$Yb_2Zr_2O_7$	7.388	7.696	96.0

Therefore, it is not surprising that both $Sm_2Zr_2O_7$ and $(Yb_{0.1}Sm_{0.9})_2Zr_2O_7$ ceramics exhibit a pyrochlore structure. As for the other zirconate ceramics in this investigation $(Yb_xSm_{1-x})_2Zr_2O_7$ $(0.3 \le x \le 1.0)$, the ratio value of $r(Ln^{3+})/r(Zr^{4+})$ is clearly lower than 1.46, therefore the $(Yb_xSm_{1-x})_2Zr_2O_7$ $(0.3 \le x \le 1.0)$ ceramics exhibit a defect fluorite-type structure.

X-ray diffraction patterns of $(Yb_xSm_{1-x})_2Zr_2O_7$ ceramics in the 2θ range of 56–60° are shown in Fig. 1(b). The $(3\,1\,1)_F/(6\,2\,2)_{Py}$ peaks gradually shift to the high angle side for $(Yb_xSm_{1-x})_2Zr_2O_7$ ceramics when the composition changes from $x=0$ ($Sm_2Zr_2O_7$) to $x=1.0$ ($Yb_2Zr_2O_7$). The lattice parameters calculated from these peaks in relation to the defect fluorite-type unit cell are depicted in Fig. 1(c). An approximately linear decrease of the lattice parameter is observed for $(Yb_xSm_{1-x})_2Zr_2O_7$ ceramics with compositions from $x=0$ ($Sm_2Zr_2O_7$) to $x=1.0$ ($Yb_2Zr_2O_7$), which is in good agreement with Vegard's rule. It indicates that $Yb_2Zr_2O_7$ and $Sm_2Zr_2O_7$ ceramics are infinitely solid solvable. Table 1 shows relative densities of $(Yb_xSm_{1-x})_2Zr_2O_7$ ceramics sintered at 1700 °C for 10 h. Clearly, all $(Yb_xSm_{1-x})_2Zr_2O_7$ ceramics have a high relative density of more than 95%. Fig. 2 shows typical morphologies of $(Yb_xSm_{1-x})_2Zr_2O_7$ ceramics sintered at 1700 °C for 10 h. The grain size and morphology of $(Yb_xSm_{1-x})_2Zr_2O_7$ ceramics with various chemical compositions are very similar, although $Sm_2Zr_2O_7$ and $(Yb_{0.1}Sm_{0.9})_2Zr_2O_7$ ceramics have a different phase structure from $(Yb_xSm_{1-x})_2Zr_2O_7$ $(0.3 \le x \le 1.0)$ ceramics. The average grain size of $(Yb_xSm_{1-x})_2Zr_2O_7$ ceramics is several micrometers. The grain boundaries in $(Yb_xSm_{1-x})_2Zr_2O_7$ ceramics are very clean. The chemical compositions of sintered ceramics

Table 2
Chemical compositions of $(Yb_xSm_{1-x})_2Zr_2O_7$ bulk ceramics detected by EDS

Ceramic bulk materials	Mol ratio		
	Yb	Sm	Zr
$Sm_2Zr_2O_7$	0	49.6	50.4
$(Yb_{0.1}Sm_{0.9})_2Zr_2O_7$	5.0	44.8	50.2
$(Yb_{0.3}Sm_{0.7})_2Zr_2O_7$	14.8	35.2	50.0
$(Yb_{0.5}Sm_{0.5})_2Zr_2O_7$	24.9	24.8	50.3
$(Yb_{0.7}Sm_{0.3})_2Zr_2O_7$	35.2	14.7	50.1
$(Yb_{0.9}Sm_{0.1})_2Zr_2O_7$	44.7	4.9	50.4
$Yb_2Zr_2O_7$	49.7	0	50.3

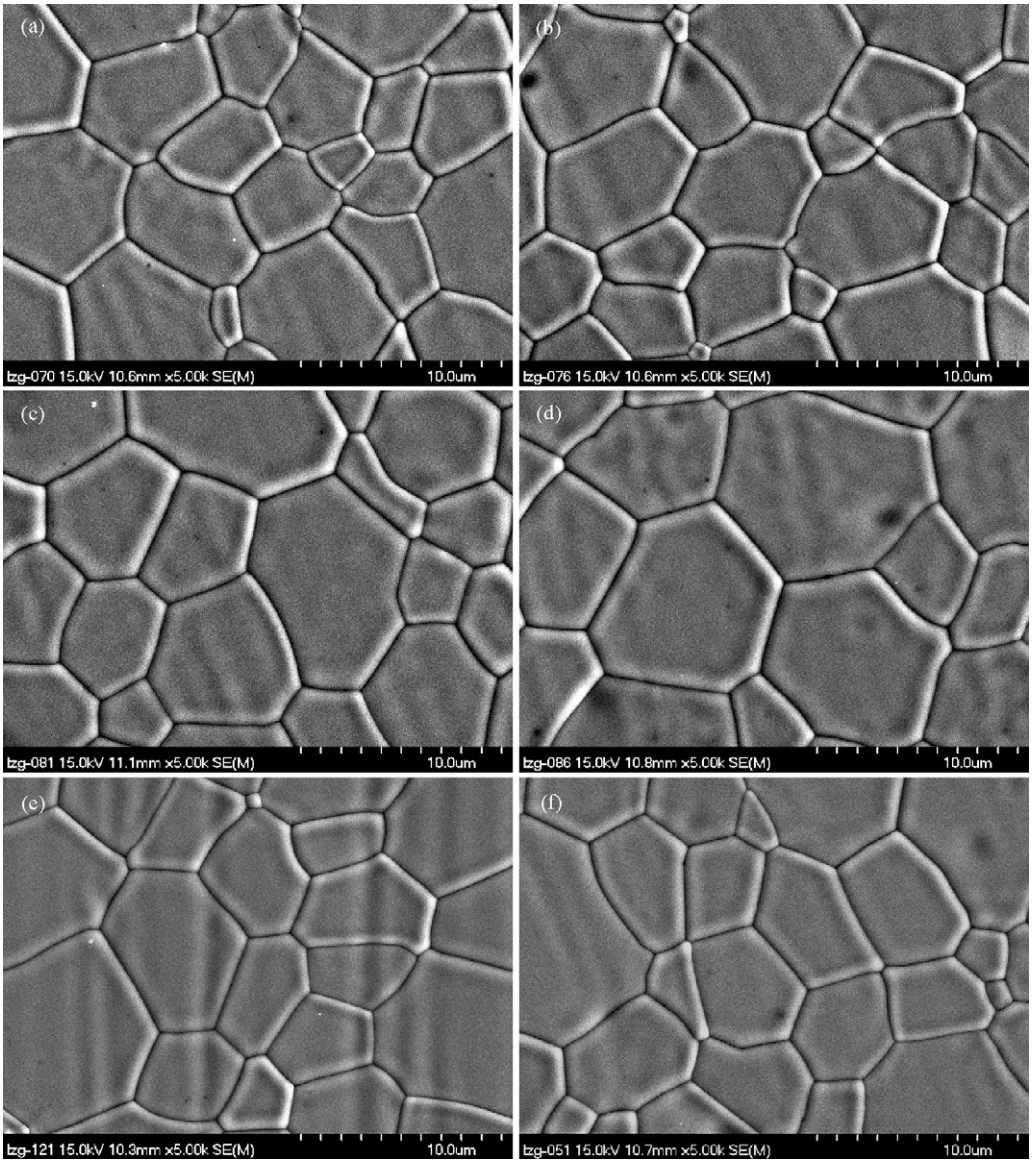

Fig. 2. Morphologies of $(Yb_xSm_{1-x})Zr_2O_7$ ceramics sintered at 1700 °C for 10 h: (a) $x = 0$; (b) $x = 0.1$; (c) $x = 0.3$; (d) $x = 0.5$; (e) $x = 0.9$; (f) $x = 1.0$.

were determined by EDS. Table 2 shows the chemical composition analyses of $(Yb_xSm_{1-x})_2Zr_2O_7$ ceramics. According to the results of EDS analysis, the mol ratios of different metallic elements in $(Yb_xSm_{1-x})_2Zr_2O_7$ ceramics are ±2% different from stoichiometry.

3.2. Thermal conductivity

The specific heat capacities of $(Yb_xSm_{1-x})_2Zr_2O_7$ ceramics calculated with the Neumann–Kopp rule at different temperatures were shown in Table 3. Table 4 shows the measured thermal

Table 3
Specific heat capacities of $(Yb_xSm_{1-x})_2Zr_2O_7$ bulk ceramics calculated with the Neumann–Kopp rule at different temperatures

Ceramic bulk materials	Specific heat capacities ($J\,g^{-1}\,K^{-1}$)							
	25 °C	200 °C	400 °C	600 °C	800 °C	1000 °C	1200 °C	1400 °C
$Sm_2Zr_2O_7$	0.380	0.443	0.472	0.491	0.506	0.519	0.532	0.544
$(Yb_{0.1}Sm_{0.9})_2Zr_2O_7$	0.378	0.440	0.468	0.487	0.502	0.515	0.528	0.540
$(Yb_{0.3}Sm_{0.7})_2Zr_2O_7$	0.372	0.433	0.462	0.480	0.494	0.508	0.520	0.532
$(Yb_{0.5}Sm_{0.5})_2Zr_2O_7$	0.367	0.427	0.455	0.472	0.487	0.500	0.512	0.524
$(Yb_{0.7}Sm_{0.3})_2Zr_2O_7$	0.362	0.421	0.448	0.466	0.480	0.493	0.505	0.517
$(Yb_{0.9}Sm_{0.1})_2Zr_2O_7$	0.357	0.415	0.442	0.459	0.473	0.486	0.498	0.509
$Yb_2Zr_2O_7$	0.355	0.412	0.439	0.456	0.470	0.483	0.494	0.506

Table 4
Measured thermal diffusivity of $(Yb_xSm_{1-x})_2Zr_2O_7$ bulk ceramics at different temperatures

Ceramic bulk materials	Thermal diffusivity ($mm^2\ s^{-1}$)							
	25 °C	200 °C	400 °C	600 °C	800 °C	1000 °C	1200 °C	1400 °C
$Sm_2Zr_2O_7$	0.771 ± 0.002	0.558 ± 0.001	0.476 ± 0.002	0.455 ± 0.003	0.438 ± 0.001	0.440 ± 0.003	0.459 ± 0.002	0.473 ± 0.004
$(Yb_{0.1}Sm_{0.9})_2Zr_2O_7$	0.704 ± 0.001	0.539 ± 0.002	0.458 ± 0.003	0.428 ± 0.001	0.416 ± 0.002	0.412 ± 0.001	0.427 ± 0.002	0.445 ± 0.003
$(Yb_{0.3}Sm_{0.7})_2Zr_2O_7$	0.658 ± 0.002	0.528 ± 0.001	0.464 ± 0.001	0.423 ± 0.001	0.411 ± 0.002	0.407 ± 0.005	0.416 ± 0.001	0.430 ± 0.002
$(Yb_{0.5}Sm_{0.5})_2Zr_2O_7$	0.619 ± 0.001	0.493 ± 0.002	0.438 ± 0.001	0.407 ± 0.003	0.396 ± 0.001	0.392 ± 0.004	0.394 ± 0.003	0.414 ± 0.002
$(Yb_{0.7}Sm_{0.3})_2Zr_2O_7$	0.633 ± 0.003	0.510 ± 0.001	0.450 ± 0.002	0.422 ± 0.003	0.405 ± 0.001	0.401 ± 0.002	0.407 ± 0.005	0.422 ± 0.003
$(Yb_{0.9}Sm_{0.1})_2Zr_2O_7$	0.671 ± 0.002	0.514 ± 0.001	0.448 ± 0.003	0.420 ± 0.001	0.404 ± 0.002	0.402 ± 0.005	0.409 ± 0.003	0.424 ± 0.005
$Yb_2Zr_2O_7$	0.720 ± 0.001	0.526 ± 0.001	0.456 ± 0.001	0.426 ± 0.004	0.409 ± 0.002	0.405 ± 0.001	0.411 ± 0.003	0.427 ± 0.004

Table 5
Calculated thermal conductivity of $(Yb_xSm_{1-x})_2Zr_2O_7$ bulk ceramics at different temperatures according to Eq. (1)

Ceramic bulk materials	Thermal conductivity ($W\ m^{-1}\ K^{-1}$)							
	25 °C	200 °C	400 °C	600 °C	800 °C	1000 °C	1200 °C	1400 °C
$Sm_2Zr_2O_7$	1.903	1.605	1.459	1.451	1.439	1.483	1.565	1.671
$(Yb_{0.1}Sm_{0.9})_2Zr_2O_7$	1.736	1.547	1.399	1.366	1.363	1.384	1.471	1.568
$(Yb_{0.3}Sm_{0.7})_2Zr_2O_7$	1.606	1.519	1.424	1.349	1.348	1.373	1.437	1.519
$(Yb_{0.5}Sm_{0.5})_2Zr_2O_7$	1.576	1.460	1.382	1.339	1.337	1.359	1.399	1.505
$(Yb_{0.7}Sm_{0.3})_2Zr_2O_7$	1.640	1.536	1.442	1.407	1.391	1.415	1.471	1.561
$(Yb_{0.9}Sm_{0.1})_2Zr_2O_7$	1.752	1.560	1.448	1.410	1.398	1.429	1.490	1.579
$Yb_2Zr_2O_7$	1.889	1.601	1.479	1.435	1.417	1.452	1.500	1.596

diffusivity of $(Yb_xSm_{1-x})_2Zr_2O_7$ bulk ceramics at different temperatures. All the values of thermal diffusivity in Table 4 are the arithmetic means of three measurements. The error derived from the mean standard deviation of three measurements for each specimen is less than 1.5%. Clearly, the thermal diffusivities of $(Yb_xSm_{1-x})_2Zr_2O_7$ ceramics monotonically decrease with increasing temperature up to 1000 °C, which is similar to most polycrystalline materials.[24] However, above 1000 °C, the thermal diffusivities of $(Yb_xSm_{1-x})_2Zr_2O_7$ ceramics show a very slight increase, which is attributed to a small contribution from radiative transport through these specimens. In this investigation, the measured thermal diffusivities of $(Yb_xSm_{1-x})_2Zr_2O_7$ ceramics are located within a range of 0.392–0.771 $mm^2\ s^{-1}$ from room temperature to 1400 °C.

According to Eq. (1), the calculated thermal conductivity of $(Yb_xSm_{1-x})_2Zr_2O_7$ ceramics before correction is shown in Table 5. The corrected thermal conductivity of $(Yb_xSm_{1-x})_2Zr_2O_7$ ceramics according to Eq. (2) and Table 1 is plotted as a function of temperature in Fig. 3. The error bars are omitted as they are smaller than the symbols. The thermal conductivity of $(Yb_xSm_{1-x})_2Zr_2O_7$ ceramics decreases gradually with increasing temperature up to 800 °C, which is attributed to the lattice thermal conduction. However, the thermal conductivities increase very slightly above 800 °C for these specimens, which may be attributed to the increased radiation contribution with increasing temperature, also known as photon thermal conductivity. From Fig. 3, co-doping of ytterbium and samarium oxides clearly reduces thermal conductivities of zirconate solid solutions over the entire temperature range, and the $YbSmZr_2O_7$ ceramics have the lowest thermal conductivity in this investigation. It is well known that the lattice thermal conductivity is proportional to the mean free path of phonon.[25]

According to above results $(Yb_xSm_{1-x})_2Zr_2O_7$ ceramics could be regarded as the solid solution of Yb^{3+} taking the site of Sm^{3+} in $Sm_2Zr_2O_7$ ceramics or Yb^{3+} is substituted by Sm^{3+} in $Yb_2Zr_2O_7$ ceramics. The smallest cation mean free path is that in which every other cation is different, as in the case of the equal molar of Yb^{3+} and Sm^{3+} in $(Yb_xSm_{1-x})_2Zr_2O_7$ system. Therefore, $YbSmZr_2O_7$ ceramics should have the lowest thermal conductivity in $(Yb_xSm_{1-x})_2Zr_2O_7$ system. The thermal conductivities of $(Yb_xSm_{1-x})_2Zr_2O_7$ ceramics in this investigation were located within the range of 1.40–1.99 $W\ m^{-1}\ K^{-1}$ from room temperature to 1400 °C, which are obviously lower than those of fully dense 7 wt.% YSZ (3.0 at room temperature to 2.3 $W\ m^{-1}\ K^{-1}$ at 700 °C reported by Wu *et al.*[10]). Thus $(Yb_xSm_{1-x})_2Zr_2O_7$ ceramics are potential candidates for thermal barrier coatings applications.

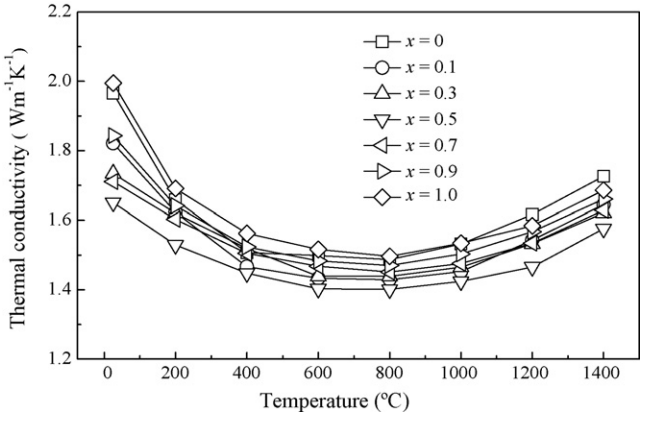

Fig. 3. The corrected thermal conductivity of $(Yb_xSm_{1-x})_2Zr_2O_7$ ceramics as a function of temperature according to Eq. (2) and Table 1.

4. Conclusions

(1) $(Yb_xSm_{1-x})_2Zr_2O_7$ ceramics were synthesized by pressureless-sintering of rare-earth zirconate powders obtained by chemical-coprecipitation and calcination method. The relative densities of $(Yb_xSm_{1-x})_2Zr_2O_7$ ceramics are higher than 95%. $Sm_2Zr_2O_7$ and $(Yb_{0.1}Sm_{0.9})_2Zr_2O_7$ ceramics exhibit a pyrochlore structure, while $(Yb_xSm_{1-x})_2Zr_2O_7$ $(0.3 \leq x \leq 1.0)$ ceramics have a defect fluorite-type structure.

(2) The thermal conductivities of $(Yb_xSm_{1-x})_2Zr_2O_7$ ceramics first gradually decrease with increasing temperature, and then slightly increase above 800 °C due to the increased radiation contribution. The thermal conductivities of $(Yb_xSm_{1-x})_2Zr_2O_7$ ceramics are located in the range of 1.40–1.99 $W\,m^{-1}\,K^{-1}$ from room temperature to 1400 °C. $YbSmZr_2O_7$ ceramics have the lowest thermal conductivity over the entire temperature range.

Acknowledgements

The authors would like to thank the financial support from the Program of Excellent Teams in Harbin Institute of Technology (HIT) and the Start-up Program for High-level HIT Faculty Returned from Abroad.

References

1. Padture, N. P., Gell, M. and Jordan, E. H., Thermal barrier coatings for gas-turbine engine applications. *Science*, 2002, **296**, 280–284.
2. Evans, A. G., Clarke, D. R. and Levi, C. G., The influence of oxides on the performance of advanced gas turbines. *J. Eur. Ceram. Soc.*, 2008, **28**, 1405–1419.
3. Zhao, X., Hashimoto, T. and Xiao, P., Effect of the top coat on the phase transformation of thermally grown oxide in thermal barrier coatings. *Scripta Mater.*, 2006, **55**, 1051–1054.
4. Cao, X. Q., Vassen, R. and Stőver, D., Ceramic materials for thermal barrier coatings. *J. Eur. Ceram. Soc.*, 2004, **24**, 1–10.
5. Andrievskaya, E. R., Phase equilibria in the refractory oxide systems of zirconia, hafnia and yttria with rare-earth oxides. *J. Eur. Ceram. Soc.*, 2008, **28**, 2363–2388.
6. Peters, M., Leyens, C., Schulz, U. and Kaysser, W. A., EB-PVD thermal barrier coatings for aeroengines and gas turbines. *Adv. Eng. Mater.*, 2003, **3**, 193–204.
7. Zhu, D. and Miller, R. A., Development of advanced low conductivity thermal barrier coatings. *Int. J. Ceram. Technol.*, 2004, **1**, 86–94.
8. Huang, X., Zakurdaev, A. and Wang, D., Microstructure and phase transformation of zirconia-based ternary oxides for thermal barrier coating applications. *J. Mater. Sci.*, 2008, **43**, 2631–2641.
9. Vassen, R., Cao, X., Tietz, F., Basu, D. and Stőver, D., Zirconates as new materials for thermal barrier coatings. *J. Am. Ceram. Soc.*, 2000, **83**, 2023–2028.
10. Wu, J., Wei, X. Z., Padture, N. P., Klemens, P. G., Gell, M., Garcia, E. *et al.*, Low-thermal-conductivity rare-earth zirconates for potential thermal-barrier-coating applications. *J. Am. Ceram. Soc.*, 2002, **85**, 3031–3035.
11. Michel, D., Perez-y-Jorba, M. and Collongues, R., Etude de la transformation ordre–desordre de la structure fluorite a la structure pyrochlore pour des phases $(1-x)ZrO_2$–xLn_2O_3. *Mater. Res. Bull.*, 1974, **9**, 1457–1468.
12. Suresh, G., Seenivasan, G., Krishnaiah, M. V. and Murti, P. S., Investigation of the thermal conductivity of selected compounds of lanthanum, samarium and europium. *J. Alloys Compd.*, 1998, **269**, L9–L12.
13. Lehmann, H., Pitzer, D., Pracht, G., Vassen, R. and Stőver, D., Thermal conductivity and thermal expansion coefficients of the lanthanum rare-earth-element zirconate system. *J. Am. Ceram. Soc.*, 2003, **86**, 1338–1344.
14. Levi, C. G., Emerging materials and processes for thermal barrier systems. *Curr. Opin. Solid State Mater. Sci.*, 2004, **8**, 77–91.
15. Mansal, N. P. and Zhu, D., Effects of doping on thermal conductivity of pyrochlore oxides for advanced thermal barrier coatings. *Mater. Sci. Eng. A*, 2007, **459**, 192–195.
16. Swalin, R. A., *Thermdynamics of Solids* (*second ed.*). John Wiley & Sons, New York, 1972, pp. 53–87.
17. Kubaschewsji, O., Alcock, C. B. and Spencer, P. J., *Materials Thermochemistry* (*sixth ed.*). Pergamon Press, Oxford, 1993, pp. 257–323.
18. Patwe, S. J., Ambekar, B. R. and Tyagi, A. K., Synthesis, characterization and lattice thermal expansion of some compounds in the system $Gd_2Ce_xZr_{2-x}O_7$. *J. Alloys Compd.*, 2005, **389**, 243–246.
19. Mandal, B. P. and Tyagi, A. K., Preparation and high temperature-XRD studies on a pyrochlore series with the general composition $Gd_{2-x}Nd_xZr_2O_7$. *J. Alloys Compd.*, 2007, **437**, 260–263.
20. Liu, Z. -G., Ouyang, J. -H., Wang, B. H., Zhou, Y. and Li, J., Preparation and thermophysical properties of $Nd_xZr_{1-x}O_{2-x/2}$ $(x = 0.1, 0.2, 0.3, 0.4, 0.5)$ ceramics. *J. Alloys Compd.*, 2008, **466**, 39–44.
21. Subramanian, M. A., Aravamudan, G. and Subba Rao, G. V., Oxide pyrochlores—a review. *Prog. Solid State Chem.*, 1983, **15**, 55–143.
22. Rohrer, G. S., *Structure and Bonding in Crystalline Materials*. Cambridge University Press, Cambridge, 2004, pp. 521–525.
23. Yamamura, H., Nishino, H., Kakinuma, K. and Nomura, K., Electrical conductivity anomaly around fluorite–pyrochlore phase boundary. *Solid State Ionics*, 2003, **158**, 359–365.
24. Berman, R., *Thermal Conduction in Solids*. Clarendon Press, Oxford, 1976, pp. 45–101.
25. Yang, J., In *Theory of Thermal Conductivity. In Thermal Conductivity: Theory, Properties and Applications*, ed. T. M. Tritt. Kluwer Academic/Plenum Publishers, New York, 2004, pp. 1–20.